A.Godinger, Y.Rotbaum, A.Vaz-Romero, J.A.Rodríguez-Martínez, D.Rittel. On the relation between shape imperfections of a specimen and necking growth rate under dynamic conditions. *International journal of engineering science*, vol. 119, pp. 278-287, October 2017

DOI: https://doi.org/10.1016/j.ijengsci.2017.06.020

On the relation between shape imperfections of a specimen and necking growth rate under dynamic conditions

A. Godinger[b], Y. Rotbaum[b], A. Vaz-Romero[a], J. A. Rodríguez-Martínez[a,*], D. Rittel[b]

[a] *Department of Continuum Mechanics and Structural Analysis. University Carlos III of Madrid. Avda. de la Universidad, 30. 28911 Leganés, Madrid, Spain*
[b] *Faculty of Mechanical Engineering, Technion - Israel Institute of Technology 32000 Haifa, Israel*

Abstract

In this work, the growth rate of necks formed in dynamically loaded tensile steel samples is investigated. For that purpose, a combined experimental-numerical approach, in which the experimental results are systematically compared with finite element calculations, has been developed. The specimens have a machined sinusoidal geometrical imperfection that covers the whole gauge, introducing a characteristic wavelength in the samples. For a given cross-section diameter, specimens with 6 different gauge lengths (i.e. 6 different specimen wavelengths) were tested. Using a high-speed camera, we measured the time evolution of the radial contraction of the central section of the samples (central section of the neck), thus obtaining the growth rate of the necks. The experiments show that the speed of growth of the necks increases non-linearly with the specimen wavelength (concave-downward shape) until saturation is reached for the longest tested specimens. Numerical simulations performed for the strain rates attained in the experiments (from 900 s^{-1} to 2100 s^{-1}) confirm this trend and demonstrate that the damping of short specimen wavelengths is caused by stress multiaxiality effects. Numerical simulations performed for strain rates greater than those attained in the experiments (above 7500 s^{-1}) show that long specimen wavelengths become damped by inertia effects at sufficiently high strain rates. For strain rates greater than 7500 s^{-1}, the maximum growth rate of the neck corresponds to an intermediate specimen wavelength defined by the joint action of stress multiaxiality and inertia on damping short and long wavelengths, respectively. Altogether, our experimental and numerical results suggest the existence of a specimen wavelength that, when inertia effects become important, determines the maximum growth rate of dynamic necks, in agreement with the predictions of the dynamic stability analyses developed by Molinari and co-workers (Fressengeas and Molinari, 1985, 1994; Mercier and Molinari, 2003, 2004).

Keywords:

---

[*] Corresponding author. Tel. +34 916249904; Fax: +34 916249430. E-mail address: jarmarti@ing.uc3m.es

Dynamic tension, Necking growth rate, Critical specimen wavelength, Stress multiaxiality, Inertia

---

1. Introduction

The rapid radial expansion of radially symmetric structures like rings (Grady and Benson, 1983; Gourdin, 1989; Zhang and Ravi-Chandar, 2006; Janiszewski, 2012), tubes (Goto et al., 2008; Hiroe et al., 2008; Zhang and Ravi-Chandar, 2008, 2010) or hemispheres (Mercier et al., 2010) is the most common experimental configuration used to investigate the processes of multiple necking and fragmentation of metallic materials at high strain rates. The radial symmetry of these problems minimizes the propagation of stress waves within the circumferential direction of the specimens (before the onset of necking), which allows for the inception and development of multiple localization patterns. These experimental works (e.g. Fig. 8 in Zhang and Ravi-Chandar (2008)) have shown that: (1) the number of necks incepted in the samples increases and (2) the variability in the (absolute) distance between necks decreases as the specimen expansion rate increases.

The theoretical framework originally developed by Mott (1947), which postulates that the distribution of necks is directly connected to the statistical material property and microstructure variations, has been traditionally used to rationalize previous experimental observations, see for instance Zhang and Ravi-Chandar (2008). It was explained that the number of necks increases and the distance between necks decreases with the loading rate because the unloading waves that emanate from the localization points propagate a shorter distance as the expansion rate increases. This allows for the activation of a larger number of material defects, which lead to a larger number of necks, as the loading rate increases.

An alternative theoretical framework was developed by Molinari and co-workers (Fressengeas and Molinari, 1985, 1994; Mercier and Molinari, 2003, 2004; Mercier et al., 2010) who approached the multiple necking problem using dynamic stability analyses. The technique consists of adding a small perturbation to the fundamental solution of the problem to determine whether a neck-like deformation field can exist (Guduru and Freund, 2002). This method predicts that the perturbation only grows for a finite number of wavelengths: short wavelengths (short necks) are damped by stress multiaxiality effects and long wavelengths (long necks) by inertia. It was concluded that the growing wavelength modes define the range of neck sizes (i.e. neck spacings) that can be found in the localization pattern. The specific wavelength mode that grows the fastest, referred to as the critical wavelength, is assumed to determine the average neck spacing in the localization pattern. The dynamic stability analyses complement the classical statistical theory of Mott (1947) and identify a deterministic component within the mechanisms which control the inception and development of the multiple necking pattern.

The predictions of the dynamic stability analyses have been confirmed, using finite element calculations, in various recent works. Rodríguez-Martínez et al. (2013b) simulated the ring expansion problem including in the outer perimeter of the samples an array of periodic (neck-like) geometric imperfections of predefined amplitude and wavelength. In agreement with the stability analyses, the numerical computations showed that sufficiently long wavelength imperfections are completely suppressed by inertia and sufficiently short wavelength imperfections are completely suppressed by stress multiaxiality effects. Furthermore, using a unitary axisymmetric cell model which included a sinusoidal spatial imperfection, Rodríguez-Martínez et al. (2013a) also demonstrated the existence of a wavelength mode that, at high strain rates, determines the minimum investment of energy to trigger a neck. It was suggested that this specific wavelength mode possesses definite resemblance with the so-called critical wavelength obtained in the linear stability analyses. Nevertheless, the numerical results obtained from the unitary cell calculations have never been compared with experiments of the same kind, and this is the scientific gap that we aim to cover with our research.

In this paper we present the first unitary cell experiments ever performed to assess whether, in agreement with the unitary cell calculations and the linear stability analysis, there are specific wavelength modes that grow faster than others (i.e. require less energy to develop). For that purpose, we have tested using a Kolsky tensile apparatus steel cylindrical specimens which include a sinusoidal imperfection that mimics the geometrical wavelength included in the unitary cell calculations (Rodríguez-Martínez et al., 2013a). Various specimen sizes, i.e. various specimen wavelengths, have been tested. In all the tests performed the neck is incepted in the central section of the sample, where the amplitude of the imperfection is maximum. The experiments have been recorded using a high-speed camera which enabled to measure the time evolution of the radial contraction of the neck. The key result of this paper is to show experimentally that the rate of growth of the necks depends on the specimen wavelength. Moreover, we have compared our experimental results with unitary cell calculations for different strain rates that we have specifically developed for this purpose. The comparison shows, in agreement with earlier theoretical and numerical works (Xue et al., 2008; Rodríguez-Martínez et al., 2017) that, when inertia effects become important, there are specific wavelengths which require less investment of energy to develop a neck.

2. Experimental setup

The dynamic tensile experiments were performed using a standard 12.7 *mm* diameter Kolsky tensile apparatus (Kolsky, 1949; Harding et al., 1960) made of hardened C300 Maraging steel bars. The apparatus was loaded using a 400 *mm* long tubular projectile, launched toward a flange located at the end of the incident bar. In order to prevent specimen reloading, a momentum trap was brought initially in contact with the loaded flange of the incident bar, whose length was identical to that of the projectile bar. Additional details of the experimental arrangement can be found in (Rittel et al., 2014; Rotbaum and Rittel, 2014).

The experimental specimens were machined from SAE 12L13 free cutting steel bars in as-received condition. As illustrated in Fig. 1, the cylindrical samples (round cross-section) used in the experiments have a sinusoidal geometrical imperfection generated during the machining process. As mentioned in the introduction, we aim to reproduce experimentally the numerical model used in Rodríguez-Martínez et al. (2013a) to identify the existence of a neck size that minimized the energy required to trigger material failure under dynamic tension. The geometrical imperfection is described by the following expression:

$$\Phi = \Phi_0 - \delta \left(1 + \cos\left(\frac{2\pi Z}{L_0}\right)\right) \tag{1}$$

where Z is the axial coordinate, L_0 is the length of the gauge, Φ_0 and Φ are the maximum and minimum cross-section diameters of the sample, and δ is the amplitude of the imperfection. Note in Fig. 1 that the origin of the cylindrical coordinate system is located in the center of the specimen. For all the specimens tested $\Phi_0 = 4$ *mm* and $\delta = 0.1$ *mm*, which leads to a normalized amplitude of the imperfection of $\Delta(\%) = 2\delta/\Phi_0 \cdot 100 = 5\%$. This large imperfection amplitude ensured that the neck developed in the center of the specimen for all the tests performed (unlike what we observed in samples without imperfections (Osovski et al., 2013; Rittel et al., 2014)). Six different gauge lengths were tested: 4, 8, 12, 16, 20 and 24 *mm*. Therefore, the length to diameter ratio of the specimens used in the experiments varies from 1 to 6. From now on, this ratio will be referred to as *specimen wavelength* and denoted by $\bar{L} = \frac{L_0}{\Phi_0}$. For each specimen wavelength, we have carried out 5 repetitions and obtained, at least, 3 successful experiments. One should note the experimental restrictions on the choice of the specimen lengths. For specimen wavelengths shorter than 1, the fillets that connect the gauge and the shoulders of the sample are substantially deformed during the loading, which invalidates the experiments. On the other hand, for specimen wavelengths greater than 6, the experimentally imparted displacement (velocity) is insufficient to fully develop specimen necking and fracture.

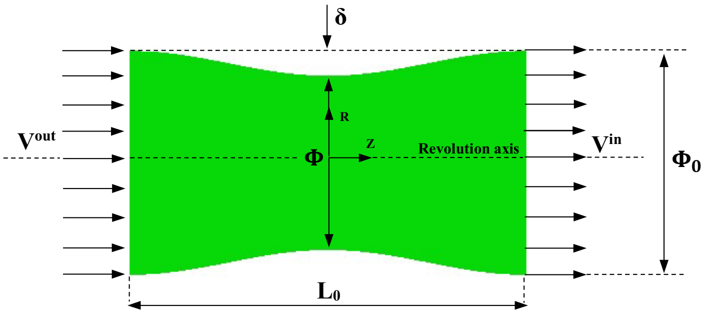

Maximum specimen diameter Φ_0 [mm]	Maximum specimen diameter Φ [mm]	Imperfection amplitude δ [mm]
4	3.8	0.1

Specimens gauge lengths L_0 [mm]					
4	8	12	16	20	24

Figure 1: Schematic representation of the gauge of the specimens. The dimensions of gauge length, maximum and minimum cross section diameters and amplitude of the imperfection are given. The amplitude of the imperfection has been increased in the sketch for a better illustration of the sinusoidal shape of the gauge. The mechanical boundary conditions of the specimens used in the dynamic tensile experiments, V^{out} and V^{in}, are also indicated.

The input and output applied velocities (mechanical boundary conditions V^{in} and V^{out} of the tests) were determined from the measured incident, reflected and transmitted pulses, as for any other standard test with the Split Hopkinson Tensile Bar. Note that Osovski et al. (2013) showed that this apparatus leads to applied velocities at both ends of the sample. The nominal strain rate in the experiments ranged between 2100 s^{-1} for the shortest specimens and 900 s^{-1} for the longest ones. The experimental restrictions mentioned above made impossible to attain strain rates close to 2000 s^{-1} for the samples longer than $\bar{L} > 3$.

Moreover, a Kirana ultra high speed digital camera was synchronized with the incident bar signals to measure the radial displacement of the central section of the sample u_R as a function of the loading time t and thus obtain the growth rate of the neck. As described in our previous work (Vaz-Romero et al., 2016), the methodology developed to measure the radial displacement of the necked section consists of 2 steps:

1. Determination and upgrade of the central cross-section of the specimen: we assume that the specimen deforms axisymmetrically in order to focus our attention (only) on half of the sample. The area of interest is upgraded using Photoshop CS6. The resolution of the original and upgraded photographs is 924 × 768 and 2000 × 475, respectively.
2. Identification of the current specimen radius using an edge detection technique: a MATLAB code was developed to detect the contour of the specimen. We scanned each of the vectors making up

the photograph and counted the pixels from the longitudinal axis of the sample to the edge. The minimum number of pixels corresponds to the center of the neck. Since the size of the pixels is known, the number of pixels provides the cross-section diameter of the neck.

The goal is to identify whether the growth rate of the neck depends on the specimen wavelength. The faster the growth rate of the neck, the more prone the material to develop necking instabilities for that specific wavelength.

3. Finite element model

We performed finite element computations using the comercial software ABAQUS/Explicit (2012) in order to complement the experimental results and check whether the experimental trends are reproduced numerically. The goal of the numerical calculations is not to mimic the experimental tests, for which we should develop a complete numerical model of the whole experimental setup, but rather to shed light into the mechanisms which control the interplay between necking growth rate and specimen wavelength. For that purpose, simple geometrical models which solely consider the gauge of the sample are sufficient, as further demonstrated in section 5. This greatly simplifies the interpretation of the finite element results and reduces the computational cost. Therefore, the geometry and dimensions of the numerical models are those presented in Fig. 1. The six specimen wavelengths used in the experiments were modelled.

Two different sets of initial and boundary conditions were used in the simulations. For the coordinate system shown in Fig. 1, these are defined as follows.

- Set 1: sample initially at rest and unstressed. These initial and boundary conditions are similar to the experimental ones.
  - Initial conditions

$$V_Z(R, Z, 0) = 0; \quad V_R(R, Z, 0) = 0; \quad \bar{\sigma}(R, Z, 0) = 0$$

where V_Z is the axial velocity, V_R the radial velocity and $\bar{\sigma}$ the equivalent stress.

  - Boundary conditions

$$V_Z(R, -L_0/2, t) = 0; \qquad V_Z(R, L_0/2, t) = V^{in} - V^{out} = \dot{\bar{\varepsilon}}_0 L_0$$

where $\dot{\bar{\varepsilon}}_0$ is the equivalent nominal strain rate.

The difference between experiments and these calculations is that in the simulations we only apply velocity in one side of the gauge while the other side is fixed axially. Nevertheless, note that this simply removes the translation (rigid body motion) to which the specimen is subjected in the tests.

- Set 2: sample subjected to initial velocity and stress fields. These initial and boundary conditions are used to explore the effect of inertia in the growth rate of the neck. The initialization of the velocity and stress fields allows to minimize the intervention of wave propagation within the specimen and attain very high strain rates with the neck always developing in the center of the sample.
  - Initial conditions

$$V_Z(R, Z, 0) = \frac{V^{in} - V^{out}}{L_0} Z = \dot{\bar{\varepsilon}}_0 Z; \qquad V_R(R, Z, 0) = -\frac{V^{in} - V^{out}}{2L_0} R = -\frac{\dot{\bar{\varepsilon}}_0}{2} R$$

$$\bar{\sigma}(R, Z, 0) = \sigma_y|_{\bar{\varepsilon}^p = 0}$$

where $\sigma_y|_{\bar{\varepsilon}^p=0}$ is the the initial yield stress of the material.

  - Boundary conditions

$$V_Z(R, \pm L_0/2, t) = \pm\frac{V^{in} - V^{out}}{2} = \pm\frac{\dot{\bar{\varepsilon}}_0 L_0}{2}$$

Note that the initial conditions require symmetric boundary conditions with respect to the central section of the sample.

The initial velocity field, consistent with the boundary conditions, allows to obtain *almost constant* strain rate along the sample since the beginning of loading. Note that the strain rate is not *fully constant* because of the inclusion of the geometrical imperfection. The initial stress field, which considers that the material has reached the yield point, minimizes the generation of elastic waves due to the sudden deformation induced in the specimen by the boundary conditions.

The material was modelled using Mises plasticity and a simple strain hardening law of the type $\sigma_y = A + B(\bar{\varepsilon}^p)^n$ where $\bar{\varepsilon}^p$ is the equivalent plastic strain. The material parameters $A = 257.5\ MPa$ (initial yield stress $\sigma_y|_{\bar{\varepsilon}^p=0}$), $B = 398.5\ MPa$ and $n = 0.071$ have been obtained fitting a tensile experiment conducted with the Split Hopkinson Tensile Bar at $2000\ s^{-1}$. Thermal and rate sensitivity effects were not considered in our modelling. The initial density of the material is $\rho = 7740\ kg/m^3$, the Young's modulus $E = 200\ GPa$ and the Poisson's ratio $\nu = 0.33$.

The finite element models are meshed using four node axisymmetric elements, with reduced integration and hourglass control (CAX4R in ABAQUS notation). The elements have an initial aspect ratio close to $1:1$ with dimensions $\approx 100 \times 100\ \mu m^2$ for all the models. Note that the ratio of the elements is not exactly $1:1$ because of the inclusion of the geometrical imperfection. A mesh convergence study was performed, in which the time evolution of different critical output variables, namely stress, strain and necking growth rate, was compared against a measure of mesh density until the results converged satisfactorily. Note that inertia acts as a potent regularization factor that contributes to the well-possessedness of the problem at hand (Knoche and Needleman, 1993; Molinari, 1997). We assume that this minimizes the spurious influence of the mesh in the solution of the boundary value problem.

4. Salient experimental outcomes

In this section of the paper we present the main outcomes of the experiments. Fig. 2 shows the normalized radial displacement of the central section of the neck $\bar{u}_R = \frac{2u_R}{\Phi_0 - 2u_R}$ (as defined by Vaz-Romero et al. (2016)) versus the normalized loading time $\bar{t} = \dot{\bar{\varepsilon}}_0 t$ (nominal strain) for the six specimen wavelengths investigated: (a) $\bar{L} = 1$, (b) $\bar{L} = 2$, (c) $\bar{L} = 3$, (d) $\bar{L} = 4$, (e) $\bar{L} = 5$ and (f) $\bar{L} = 6$. While we performed 5 repetitions for each specimen wavelength, in the plots we only show $2-3$ tests for the sake of clarity. Note the high repeatability in our measurements since, for most of the wavelengths investigated, the data corresponding to different experiments practically overlap each other. This proves the robustness of the method developed to record the radial displacement of the central section of the neck (described in section 2). The strain rate indicated in each plot corresponds to the average of the tests shown for each wavelength. For a given specimen wavelength, the tests performed never showed differences in the applied strain rate that are greater than 150 s^{-1}, i.e. the average strain rate reported is representative of all the tests conducted for a given wavelength. Moreover, as mentioned in section 2, the strain rate decreases with the specimen wavelength. We acknowledge that this influences inertia effects, which decrease with the strain rate decrease, and thus affects the rate of development of the neck (Fressengeas and Molinari, 1985; Mercier and Molinari, 2003, 2004). Nevertheless, we claim that our experimental results for different specimen wavelengths can still be compared each other to offer a consistent picture of the influence of the specimen wavelength in the necking growth rate. This assumption is supported by Fig. 6, which shows a comparison between the numerical results obtained with (1) the actual strain rates attained in the experiments for the different samples sizes and (2) an initial strain rate of 5000 s^{-1} constant for all the sample lengths. The comparison yielded similar results which suggests that strain rate plays a secondary role in the necking growth rates obtained from the experiments.

Moreover, one should note that all the experimental $\bar{u}_R{-}\bar{t}$ curves show a characteristic concave-upward shape. During the first stages of loading the radial displacement of the center of the sample is close to the fundamental solution illustrated by the green solid line. The fundamental solution is calculated assuming that the specimen has initially a constant cross-section area, deforms homogeneously and is incompressible. At a given loading time, the radial displacement measured in the experiments deviates from the fundamental solution, which indicates the onset of the localized necking instability (Rodríguez-Martínez et al., 2013a). The portion of the $\bar{u}_R - \bar{t}$ curve after the necking inception, usually referred to as the post-critical regime, represents the development of the neck. The dimensionless time (nominal strain) corresponding to the inception of the localized neck decreases rapidly with the specimen wavelength for short values of $\bar{L}$ $(1, 2)$ and becomes rather independent of the specimen wavelength for large values of $\bar{L}$ $(\geqslant 4)$. For specimen wavelengths equal or greater than 4, the experimental data deviate from the fundamental solution very early in the loading process, i.e. the localized neck is incepted very early in the loading process. Therefore, our experiments prove that the strain which determines the onset of the localized neck depends on the specimen wavelength, as it was shown numerically, for instance, by Xue et al. (2008) and Rodríguez-Martínez et al. (2013a).

Moreover, we can estimate the normalized growth rate of the neck $\dot{\bar{u}}_R$ using a linear approximation to the post-critical portion of the $\bar{u}_R - \bar{t}$ curve (slopes indicated in Fig. 2). Note that we linearize for the larger values of $\bar{u}_R$ obtained the experiments. The normalized (and linearized) growth rate of the neck possesses definite resemblance with the normalized perturbation growth rate used in the linear stability analyses to quantify the susceptibility of materials to develop necking instabilities (Fressengeas and Molinari, 1994; Zhou et al., 2006; Mercier and Molinari, 2003).

Fig. 3 shows the growth rate of the neck versus the specimen wavelength. Note that the shape of our experimental $\dot{\bar{u}}_R - \bar{L}$ curve is similar to the shape of the analytical $\bar{\eta}^+ - \bar{L}$ curves reported in Fig. 16 in (Rodríguez-Martínez et al., 2013a), where $\bar{\eta}^+$ is the normalized perturbation growth rate. Our experiments, in agreement with the predictions of the linear stability analysis, show that the growth rate of the neck is small for short values of $\bar{L}$. This is caused by the stabilizing effect of stress multiaxiality on short wavelengths (Zhou et al., 2006; Rodríguez-Martínez et al., 2013b). As the specimen wavelength increases, the growth rate of the neck increases too, until a kind of maximum for $\dot{\bar{u}}_R$ seems to be reached for a wavelength between 5 and 6. However, the maximum of the experimental curve is very weak, in contrast with the strong maximum shown by the analytical curves reported in Fig. 16 of Rodríguez-Martínez et al. (2013a). In addition, the maximum in the analytical curves is followed by a decreasing branch which is not captured by our experiments. Such disagreement between experiments and analytical predictions is caused by the *relatively small* strain rates that could be reached in our tests due to the experimental limitations described in section 2. Note that the strain rates reported in Fig. 16 of Rodríguez-Martínez et al. (2013a) are, at least, one order of magnitude greater than the strain rates we obtained in the tests. We assume that the increase of the strain rate in our experiments would boost inertia effects and these, in turn, would slow down the growth rate of long wavelengths. This would lead to a stronger maximum in the experimental $\dot{\bar{u}} - \bar{L}$ curve that, based on the results of Rodríguez-Martínez et al. (2013a), should occur for smaller values of $\bar{L}$ (smaller than 5 or 6). In order to check this hypothesis, in the following sections of the paper we use finite element calculations performed with the numerical configurations described in section 3.

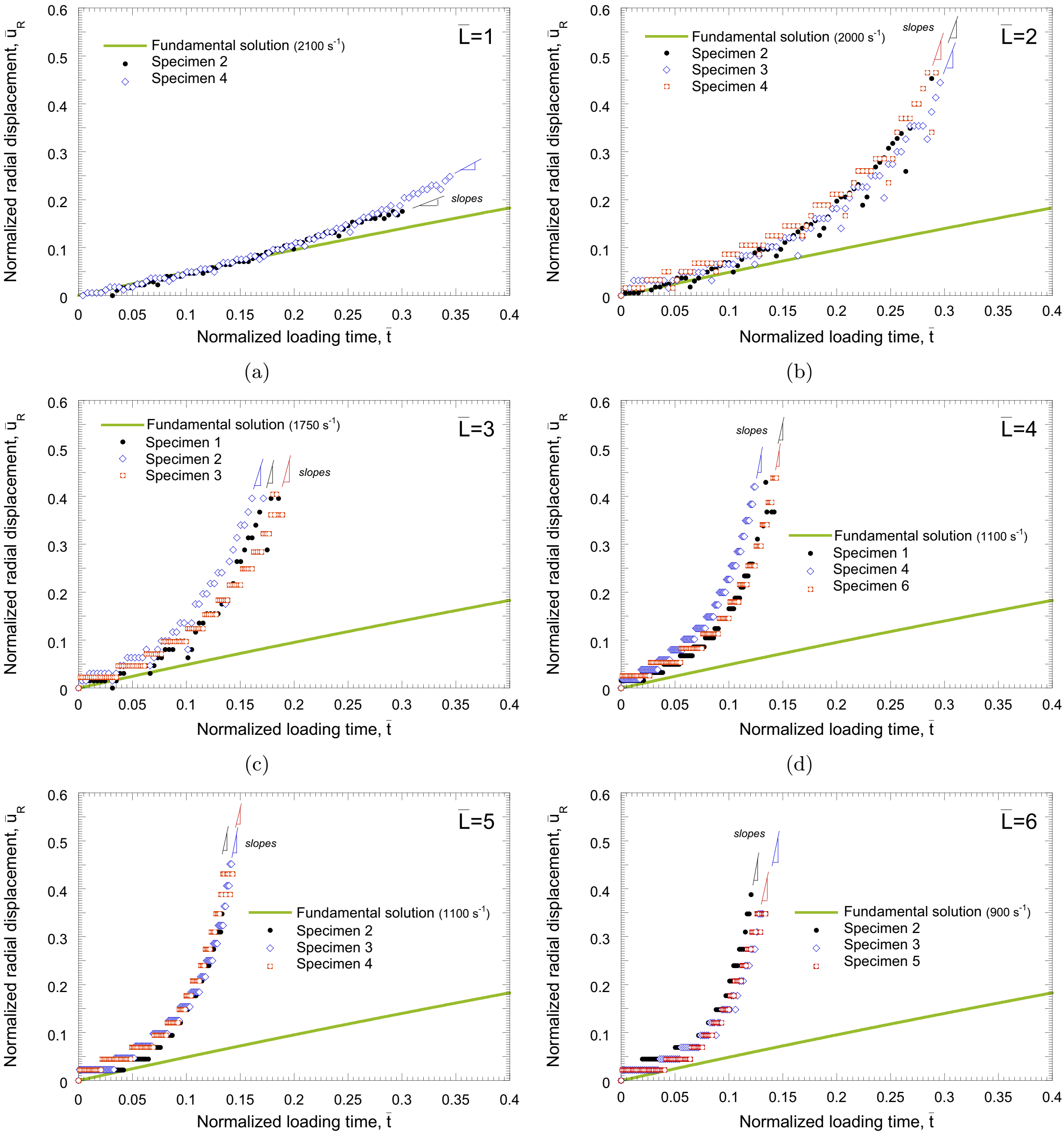

(a) (b)

(c) (d)

(e) (f)

Figure 2: Experiments. Normalized radial displacement of the central section of the neck $\bar{u}_R$ versus normalized loading time $\bar{t}$ for the six sample sizes investigated. (a) Specimen wavelength $\bar{L} = 1$. Two experiments reported with average initial (nominal) strain rate $\dot{\bar{\varepsilon}}_0 = 2100\ s^{-1}$. (b) Specimen wavelength $\bar{L} = 2$. Three experiments reported with average initial strain rate $\dot{\bar{\varepsilon}}_0 = 2000\ s^{-1}$. (c) Specimen wavelength $\bar{L} = 3$. Three experiments reported with average initial strain rate $\dot{\bar{\varepsilon}}_0 = 1750\ s^{-1}$. (d) Specimen wavelength $\bar{L} = 4$. Three experiments reported with average initial strain rate $\dot{\bar{\varepsilon}}_0 = 1100\ s^{-1}$. (e) Specimen wavelength $\bar{L} = 5$. Three experiments reported with average initial strain rate $\dot{\bar{\varepsilon}}_0 = 1100\ s^{-1}$. (f) Specimen wavelength $\bar{L} = 6$. Three experiments reported with average initial strain rate $\dot{\bar{\varepsilon}}_0 = 900\ s^{-1}$.

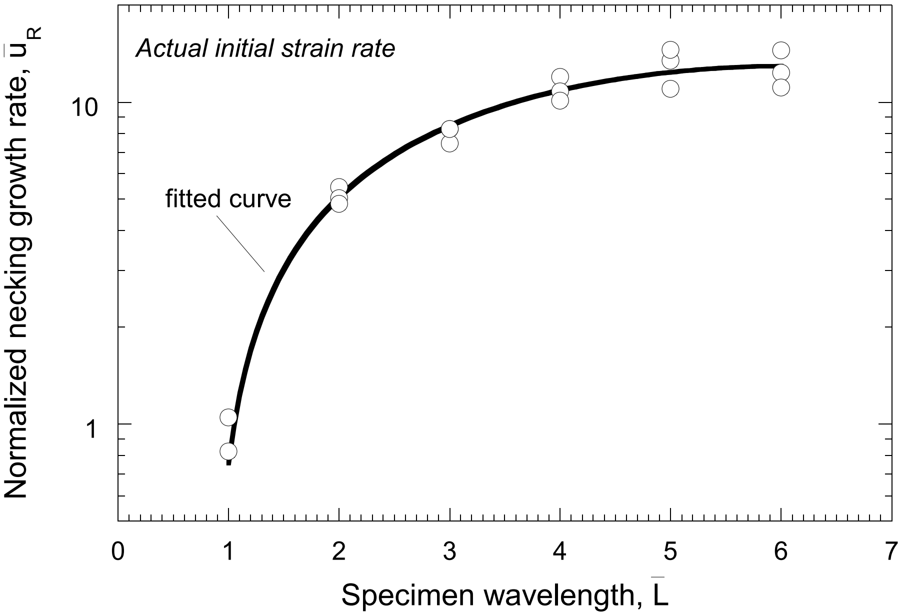

Figure 3: Experiments. Normalized growth rate of the neck $\dot{\bar{u}}_R$ versus specimen wavelength $\bar{L}$. The normalized growth rate is calculated using the average strain rate corresponding to each specimen wavelength.

5. Analysis and results: comparison between experiments and finite element calculations

We compare the normalized growth rate of the neck $\dot{\bar{u}}_R$ obtained from the experiments with the numerical results obtained from simulations performed for different imperfection amplitudes, the two sets of initial and boundary conditions described in section 3 and various strain rates.

5.1. Influence of the imperfection amplitude

Fig. 4 shows the curve fitted to the experiments presented in Fig. 3 and the results obtained from numerical calculations conducted with three different imperfection amplitudes: $\Delta = 5\%$ (as in the experiments), $\Delta = 2.5\%$ and $\Delta = 1.25\%$. We also show the finite element results obtained from simulations in which no imperfection was included, $\Delta = 0\%$. The numerical values of $\dot{\bar{u}}_R$ have been obtained as in the experiments: we plotted the normalized radial displacement of the central section of the neck against the normalized loading time and then linearise the post-critical regime for the maximum values of $\bar{u}_R$ obtained in the experiments. In the numerical calculations we use the initial and boundary conditions denoted as set 1: the specimen is at rest and unstressed, as in the experiments.

The numerical estimations of the normalized growth rate of the neck show good agreement with the experimental results (despite the simple constitutive model used in the computations). The finite element calculations also predict an increase of $\dot{\bar{u}}_R$ with $\bar{L}$ which is important for short wavelengths but becomes mild for the larger values of $\bar{L}$ investigated. Note that the numerical results presented in Fig. 4 are rather independent of the imperfection amplitude, which seems to play a secondary role in the growth rate of the neck (at least for the cases analysed in this work). We have checked for all the values of Δ investigated in this paper that the imperfection significantly affects the strain which determines the onset of the localized necking instability (which decreases with the amplitude as reported by Rodríguez-Martínez et al. (2013a, 2017)), but it barely affects the necking growth rate.

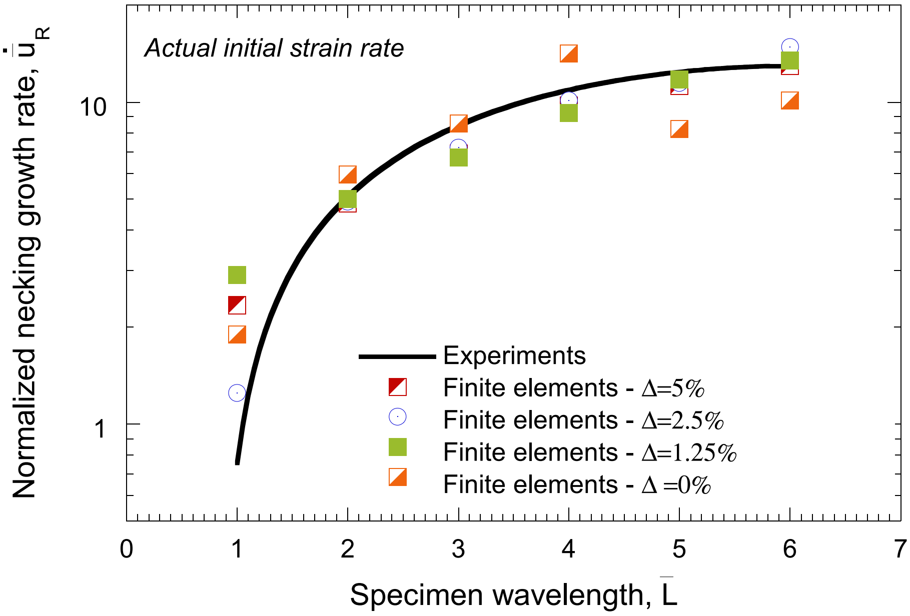

Figure 4: Comparison between experiments and finite elements. Normalized growth rate of the neck $\dot{\bar{u}}_R$ versus specimen wavelength $\bar{L}$. The normalized growth rate is calculated using the average strain rate corresponding to each specimen wavelength. The numerical simulations are conducted for three different imperfection amplitudes: $\Delta = 5\%$ (as in the experiments), $\Delta = 2.5\%$ and $\Delta = 1.25\%$. We also include the numerical results obtained from simulations in which no imperfection was included $\Delta = 0\%$. In the numerical calculations we use the initial and boundary conditions denoted as set 1: the specimen is at rest and unstressed, as in the experiments.

5.2. Influence of initial conditions

Fig. 5 shows the curve fitted to the experiments presented in Fig. 3 and the results obtained from numerical calculations performed with the two different sets of initial and boundary conditions introduced in section 3: (1) sample initially at rest and unesstressed, and (2) sample subjected to initial velocity and stress fields. The amplitude of the imperfection included in the numerical models is $\Delta = 5\%$, as in the experiments. We observe that, for the strain rates attained in the experiments, the initialization of the stress and velocity fields does not lead to meaningful differences in the numerical results. Nevertheless, we have checked that at higher strain rates the initial conditions do play a key role in the outcomes of the numerical simulations. When the initial strain rate approaches 4000 s^{-1}, if the sample is initially at rest and unstressed, the neck does not develop in the center of the sample for the longest specimens tested, but at the end where the velocity is applied. Similar behaviour was observed experimentally in (Osovski et al., 2013; Rittel et al., 2014). This is because the stress wave generated by the loading velocity is sufficiently intense to trigger the neck (Xue et al., 2008). In other words, the so-called critical impact velocity has been attained (Klepaczko, 2005; Rusinek et al., 2005). Then, the length of the sample virtually plays no role in the results (the specimen behaves as a kind of semi-infinite solid) which impedes the assessment of the influence of the specimen wavelength on the necking growth rate. However, initializing the velocity and stress fields, as described in section 3, minimizes the propagation of stress waves within the specimen due to the application of the boundary conditions and avoids the appearance of the critical impact velocity (Rodríguez-Martínez et al., 2013a; Zaera et al., 2014). We have checked that, for all the strain rates and specimen wavelengths investigated in this work, the initialization of the stress and velocity fields leads to the inception of the neck in the centre of the sample. Therefore, application of these boundary conditions does allow to assess the influence of the specimen wavelength on the necking growth rate at very high strain rates (Rodríguez-Martínez et al., 2013a). This is conducted in the following section.

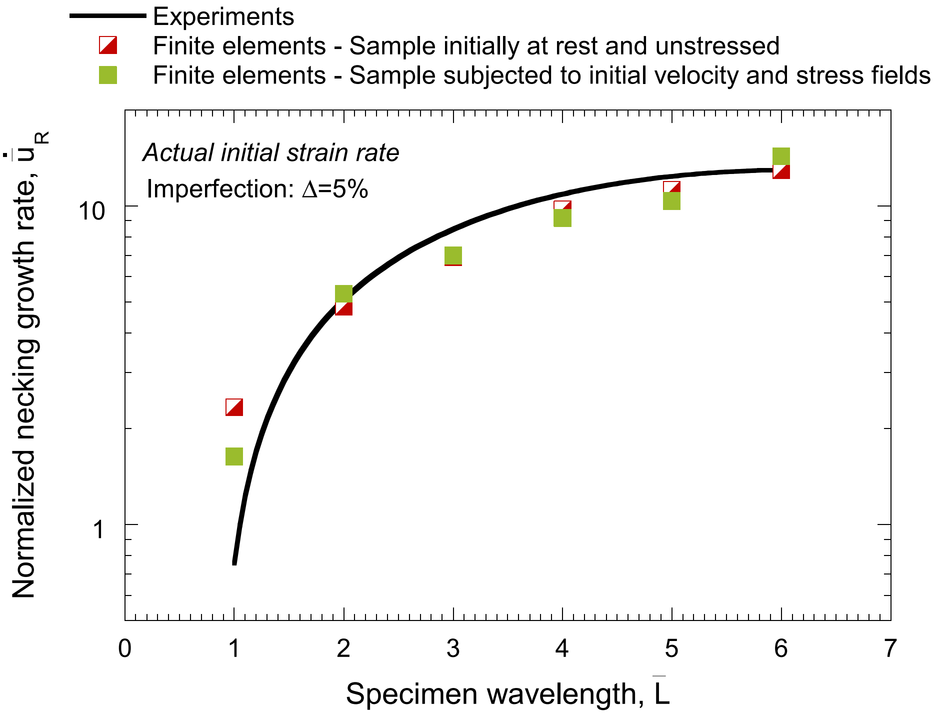

Figure 5: Comparison between experiments and finite elements. Normalized growth rate of the neck $\dot{\bar{u}}_R$ versus specimen wavelength $\bar{L}$. The normalized growth rate is calculated using the average strain rate corresponding to each specimen wavelength. The numerical simulations are conducted for the two different sets of initial and boundary conditions introduced in section 3: (1) sample initially at rest and unstressed, and (2) sample subjected to initial velocity and stress fields. The amplitude of the imperfection included in the numerical simulations is $\Delta = 5\%$, as in the experiments.

5.3. *Influence of strain rate*

Fig. 6 shows the curve fitted to the experiments presented in Fig. 3 and the results obtained from numerical calculations performed for four different initial (nominal) strain rates: 5000 s^{-1}, 7500 s^{-1}, 10000 s^{-1} and 20000 s^{-1}. We have also included the numerical results obtained for the experimental strain rates previously reported in Fig. 5. All the numerical calculations are conducted with the second set of initial and boundary conditions defined in section 3 in which the sample is subjected to initial velocity and stress fields. The amplitude of the imperfection included in the numerical simulations is $\Delta = 5\%$, as in the experiments.

For the nominal strain rate 5000 s^{-1} the numerical values are close to the experimental results and to the numerical results obtained for the experimental strain rates. It seems that for the experimental strain rates and also for 5000 s^{-1} (and the specimen cross-section and lengths used in this work) inertia does not play a meaningful role in the growth rate of the neck. For 7500 s^{-1} the numerical values start to deviate from the experimental results and from the numerical calculations performed for both the experimental strain rates and 5000 s^{-1}. We observe a maximum in the necking growth rate for $\bar{L} = 5$. This value of $\bar{L}$ defines the specimen wavelength which requires the smallest investment of energy to develop a neck, the so-called critical wavelength in Rodríguez-Martínez et al. (2013a, 2017). Inertia effects start to be important for 7500 s^{-1}, which slows down the growth rate of long wavelengths. For 10000 s^{-1} the maximum in the $\dot{\bar{u}}_R - \bar{L}$ curve is stronger (greater curvature) and corresponds to a smaller value of the specimen wavelength $\bar{L} = 3$. An additional increase in the strain rate up to 20000 s^{-1} moves the maximum of the $\dot{\bar{u}}_R - \bar{L}$ curve to $\bar{L} = 2$. The growth rate of the neck for $\bar{L} = 1$ remains largely independent of the strain rate, since for such a short wavelength the necking development is mostly controlled by the stress multiaxiality effects for all the values of strain rate considered. It is important to note the resemblance of the numerical $\dot{\bar{u}}_R - \bar{L}$ curve obtained for 20000 s^{-1} with the analytical $\bar{\eta}^{+} - \bar{L}$ curves reported in Fig. 16 of Rodríguez-Martínez et al. (2013a). They both have identical shape: short wavelengths are damped by stress multiaxiality effects and long wavelengths by inertia. This leads to the development of an intermediate wavelength which defines the maximum growth rate of the neck, previously referred to as critical wavelength. It should also be noted that, in the numerical results of Fig. 6 and in the analytical predictions of Fig. 16 in Rodríguez-Martínez et al. (2013a), this critical wavelength decreases with increasing strain rate. These results suggest that, as we hypothesized in section 4, our experiments do not show a strong maximum in the $\dot{\bar{u}}_R - \bar{L}$ curve because the strain rate (inertia) is not large enough.

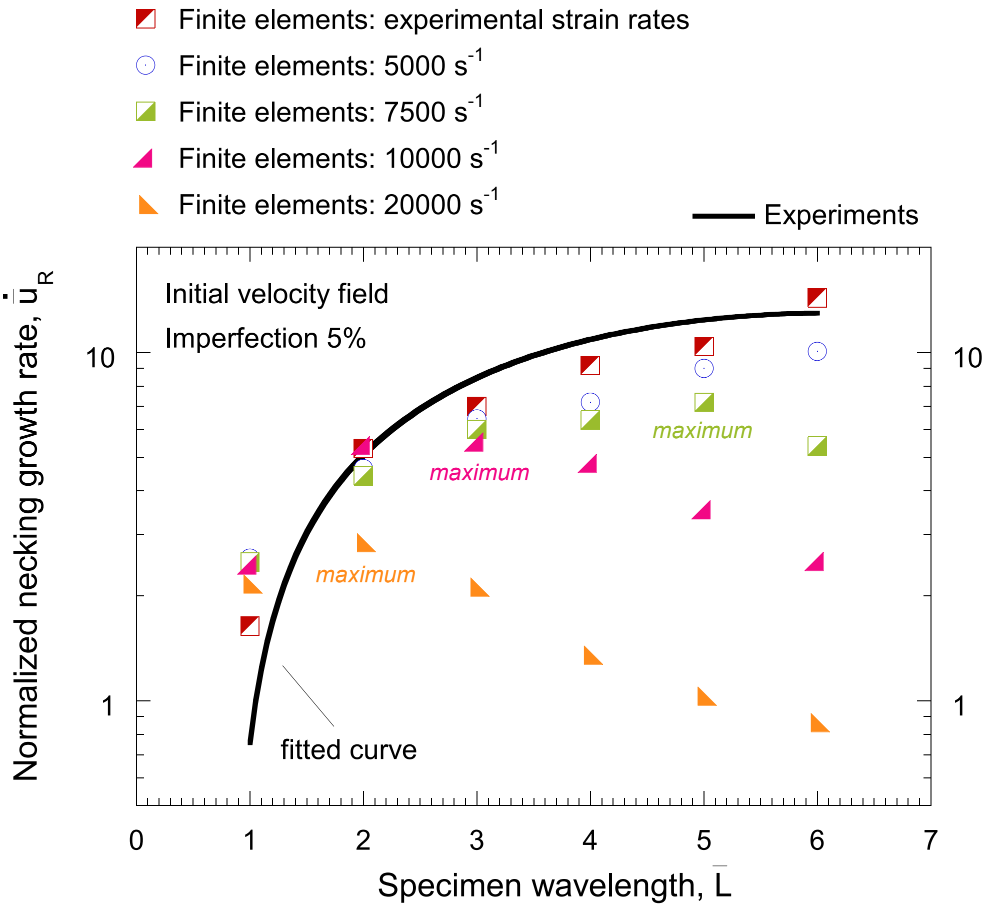

Figure 6: Comparison between experiments and finite elements. Normalized growth rate of the neck $\dot{u}_R$ versus specimen wavelength $\bar{L}$. The numerical calculations are conducted for four different initial (nominal) strain rates: 5000 s^{-1}, 7500 s^{-1}, 10000 s^{-1} and 20000 s^{-1}. We have also included the numerical results obtained for the experimental strain rates previously reported in Fig. 5. The second set of initial and boundary conditions defined in section 3 in which the sample is subjected to initial velocity and stress fields is used in all the computations. The amplitude of the imperfection included in the numerical simulations is $\Delta = 5\%$, as in the experiments.

6. Discussion and conclusions

In this paper we have developed a combined experimental-numerical approach to provide new insights into the interplay between the specimen wavelength $\bar{L}$ and the necking growth rate $\dot{u}_R$ in tensile samples subjected to dynamic tension.

The experiments, which from the authors' knowledge are the first tests of this kind ever performed, were carried out using specimens of various lengths which include a sinusoidal geometric imperfection. We have obtained that the growth rate of the neck is very small for short specimens (due to stress multiaxiality effects), gradually increases as the specimen wavelength increases, and finally reaches *a kind of maximum* for the longest samples tested. Establishing a similarity between the necking growth rate $\dot{u}_R$ obtained in the experiments and the perturbation growth rate $\bar{\eta}^+$ used in the stability analyses of Molinari and co-workers (Fressengeas and Molinari, 1994; Mercier and Molinari, 2003; Rodríguez-Martínez et al., 2013a), we observe that the experimental $\dot{u}_R - \bar{L}$ curve shows a definite resemblance with the $\bar{\eta}^+ - \bar{L}$ curve obtained analytically under quasi-static loading conditions. This suggests that the inertia effects are not playing a meaningful role in the growth rate of the necks measured in the experiments. In order to check this hypothesis we have carried out finite element simulations for strain rates equal or greater than those attained experimentally. The computations conducted for the strain rates of the tests predict necking grow rates in agreement with the experimental measurements. On the other hand, the simulations carried out for larger strain rates than those attained in the tests (above 7500 s^{-1}) show that the growth rate of necks is slowed down for long specimen wavelengths due to inertia effects. At high strain rates, the short specimen wavelengths are damped by stress multiaxiality effects and the long specimen wavelengths are damped by inertia, which leads to the promotion of an intermediate wavelength for which the neck grows the fastest. When inertia effects become important, the numerical $\dot{u}_R - \bar{L}$ curve shows a definite resemblance with the $\bar{\eta}^+ - \bar{L}$ curve obtained analytically from stability analyses under dynamic loading conditions. Altogether, the combination of the experimental and numerical results presented in this paper suggest the existence of a critical wavelength that, when inertia effects become important, determines the size of dynamic necks, in agreement with the predictions of the dynamic stability analyses developed by Molinari and co-workers (Fressengeas and Molinari, 1985, 1994; Mercier and Molinari, 2003, 2004).

Additional experimental work, in which inertia effects play a greater role, is needed to validate this hypothesis, which is so far partially supported by the experimental evidence reported in this paper.

References

ABAQUS/Explicit, 2012. Abaqus Explicit v6.12 User's Manual, version 6.12 Edition. ABAQUS Inc., Richmond, USA.

Fressengeas, C., Molinari, A., 1985. Inertia and thermal effects on the localization of plastic flow. Acta Metallurgica 33, 387–396.

Fressengeas, C., Molinari, A., 1994. Fragmentation of rapidly stretching sheets. European Journal of Mechanics A/Solids 13, 251–268.

Goto, D., Becker, R., Orzechowski, T., Springer, H., Sunwoo, A., Syn, C., 2008. Investigation of the fracture and fragmentation of explosively driven rings and cylinders. International Journal of Impact Engineering 35, 1547–1556.

Gourdin, H., 1989. Analysis and assessment of electromagnetic ring expansion as a high-strain-rate test. Journal of Applied Physics 65, 411–422.

Grady, D. E., Benson, D. A., 1983. Fragmentation of metal rings by electromagnetic loading. Experimental Mechanics 12, 393–400.

Guduru, P. R., Freund, L. B., 2002. The dynamics of multiple neck formation and fragmentation in high rate extension of ductile materials. International Journal of Solids and Structures 39, 5615–5632.

Harding, J., Wood, E. O., Campbell, J. D., 1960. Tensile Testing of Materials at Impact Rates of Strain. Journal of Mechanical Engineering Science 2, 488–96.

Hiroe, T., Fujiwara, K., Hata, H., Takahashi, H., 2008. Deformation and fragmentation behaviour of exploded metal cylinders and the effects of wall materials, configuration,explosive energy and initiated locations. International Journal of Impact Engineering 35, 1578–1586.

Janiszewski, J., 2012. Ductility of selected metals under electromagnetic ring test loading conditions. International Journal of Solids and Structures 49, 1001–1008.

Klepaczko, J. R., 2005. Review on critical impact velocities in tension and shear. International Journal of Impact Engineering 32, 188–209.

Knoche, P., Needleman, A., 1993. The effect of size on the ductility of dynamically loaded tensile bars. European Journal of Mechanics A/Solids 12, 585–601.

Kolsky, H., 1949. An investigation of the mechanical properties of materials at very high rRates of loading. Proceedings of the Physical Society. Section B 62, 676–700.

Mercier, S., Granier, N., Molinari, A., Llorca, F., Buy, F., 2010. Multiple necking during the dynamic expansion of hemispherical metallic shells, from experiments to modelling. Journal of the Mechanics and Physics of Solids 58, 955–982.

Mercier, S., Molinari, A., 2003. Predictions of bifurcations and instabilities during dynamic extensions. International Journal of Solids and Structures 40, 1995–2016.

Mercier, S., Molinari, A., 2004. Analysis of multiple necking in rings under rapid radial expansion. International Journal of Impact Engineering 30, 403–419.

Molinari, A., 1997. Collective behaviour and spacing of adiabatic shear bands. Journal of the Mechanics and Physics of Solids 45, 1551–1575.

Mott, N. F., 1947. Fragmentation of shell cases. In: . Series A. Proceedings of the Royal Society, London, pp. 300–308.

Osovski, S., Rittel, D., Rodríguez-Martínez, J. A., Zaera, R., 2013. Dynamic tensile necking: Influence of specimen geometry and boundary conditions. Mechanics of Materials 62, 1–13.

Rittel, D., Rotbaum, Y., Rodríguez-Martínez, J. A., Sory, D., Zaera, R., 2014. Dynamic necking of notched tensile bars: an experimental study. Experimental Mechanics 54, 1099–1109.

Rodríguez-Martínez, J. A., Molinari, A., Zaera, R., Vadillo, G., Fernández-Sáez, J., 2017. The critical neck spacing in ductile plates subjected to dynamic biaxial loading: On the interplay between loading path and inertia effects. International Journal of Solids and Structures 108, 74–84.

Rodríguez-Martínez, J. A., Vadillo, G., Fernández-Sáez, J., Molinari, A., 2013a. Identification of the critical wavelength responsible for the fragmentation of ductile rings expanding at very high strain rates. Journal of the Mechanics and Physics of Solids 61, 1357–1376.

Rodríguez-Martínez, J. A., Vadillo, G., Zaera, R., Fernández-Sáez, J., 2013b. On the complete extinction of selected imperfection wavelengths in dynamically expanded ductile rings. Mechanics of Materials 62, 1–13.

Rotbaum, Y., Rittel, D., 2014. Is there an optimal gauge length for dynamic tensile specimens? Experimental Mechanics 54, 1205–1214.

Rusinek, A., Zaera, R., Klepaczko, J. R., Cheriguene, R., 2005. Analysis of inertia and scale effects on dynamic neck formation during tension of sheet steel. Acta Materialia 53, 5387–5400.

Vaz-Romero, A., Rotbaum, Y., Rodríguez-Martínez, J. A., Rittel, D., 2016. Necking evolution in dynamically stretched bars: New experimental and computational insights. Journal of the Mechanics and Physics of Solids 91, 216–239.

Xue, Z., Vaziri, A., Hutchinson, J. W., 2008. Material aspects of dynamic neck retardation. Journal of the Mechanics and Physics of Solids 56, 93–113.

Zaera, R., Rodríguez-Martínez, J. A., Vadillo, G., Fernández-Sáez, J., 2014. Dynamic necking in materials with strain induced martensitic transformation. Journal of the Mechanics and Physics of Solids 64, 316–337.

Zhang, H., Ravi-Chandar, K., 2006. On the dynamics of necking and fragmentation - I. Real-time and post-mortem observations in Al 6061-O. International Journal of Fracture 142, 183–217.

Zhang, H., Ravi-Chandar, K., 2008. On the dynamics of necking and fragmentation - II. Effect of material properties geometrical constraints and absolute size. International Journal of Fracture 150, 3–36.

Zhang, H., Ravi-Chandar, K., 2010. On the dynamics of localization and fragmentation - IV. Expansion of Al 6061-O tubes. International Journal of Fracture 163, 41–65.

Zhou, F., Molinari, J. F., Ramesh, K. T., 2006. An elasto-visco-plastic analysis of ductile expanding ring. International Journal of Impact Engineering 33, 880–891.